

## Thermal Hall Effect of Magnons in Collinear Antiferromagnetic Insulators: Signatures of Magnetic and Topological Phase Transitions

Robin R. Neumann<sup>1</sup>, Alexander Mook<sup>2</sup>, Jürgen Henk<sup>1</sup>, and Ingrid Mertig<sup>1</sup>

<sup>1</sup>*Institut für Physik, Martin-Luther-Universität Halle-Wittenberg, D-06099 Halle (Saale), Germany*

<sup>2</sup>*Department of Physics, University of Basel, Klingelbergstrasse 82, CH-4056 Basel, Switzerland*



(Received 1 September 2021; accepted 21 January 2022; published 14 March 2022)

We demonstrate theoretically that the thermal Hall effect of magnons in collinear antiferromagnetic insulators is an indicator of magnetic and topological phase transitions in the magnon spectrum. The transversal heat current of magnons caused by a thermal gradient is calculated for an antiferromagnet on a honeycomb lattice. An applied magnetic field drives the system from the antiferromagnetic phase via a spin-flop phase into the field-polarized phase. In addition to these magnetic phase transitions, we find topological phase transitions within the spin-flop phase. Both types of transitions manifest themselves in prominent and distinguishing features in the thermal conductivity, which changes by several orders of magnitude. The variation of temperature provides a tool to discern experimentally the two types of phase transitions. We include numerical results for the van der Waals magnet MnPS<sub>3</sub>.

DOI: [10.1103/PhysRevLett.128.117201](https://doi.org/10.1103/PhysRevLett.128.117201)

**Introduction.**—In electronic systems, details of the electronic structure and the magnetic configuration manifest themselves in the transport properties. As an example, the quantum anomalous Hall effect, in which the transversal transport coefficient is quantized, is a clear signature of a topologically nontrivial phase. Moreover, topological phases of the electronic states can be clearly identified spectroscopically, e.g., in topological insulators [1–5].

The field of topology is not restricted to fermions, but also applies to bosons. The topological features of phonons [6–13], photons [14–18], and magnetic excitations [19–27], however, are more subtle due to the lack of the Pauli exclusion principle and quantized transport. In this Letter, we focus on magnons because they are easily manipulated by external magnetic fields. The identification of magnon edge states, the hallmarks of a nontrivial system, is notoriously difficult. On the one hand, angle-resolved photoelectron spectroscopy cannot be applied at all and spin-polarized scanning tunneling spectroscopy has severe restrictions [28–33]. On the other hand, inelastic neutron scattering succeeds in detecting gapped bulk spectra, but fails in resolving edge modes [34]. These apparent shortcomings call for identifying clear signatures of magnetic and topological phase transitions.

In this Letter, we aim at bridging the apparent gap sketched in the preceding paragraph. For this purpose, we investigate theoretically an antiferromagnet that exhibits spin-split, nonreciprocal magnon bands and both magnetic and topological phase transitions induced by an applied magnetic field. These phase transitions show up as clear characteristic signatures in the field and temperature dependence of the thermal Hall conductivity, which are explained by the magnonic band structure and the Berry

curvature. In order to convey the strong tunability and sensitivity of the thermal Hall effect, we calculate the thermal Hall magnetoconductivity at two selected phase transitions. Our findings suggest a means for identifying magnetic and topological phases via transport measurements, which could be especially attractive in two-dimensional materials, for which other methods are impractical (e.g., neutron scattering due to low signal intensities). Conversely, they insinuate a way to externally control the thermal Hall effect due to the significant changes across the phase transitions. The numerical results for MnPS<sub>3</sub>, which is known for its nontrivial magnon transport [35], ask for comparison with experimental data.

Previous reports addressed thermal Hall effects in collinear ferromagnets with Dzyaloshinskii-Moriya interaction (DMI) and dipolar interactions [19,20,24,36–61], in weak ferromagnets with scalar spin chirality or due to magnetic fields [62–76], in noncollinear antiferromagnets [77], or in paramagnets [13,42,45,62,78–83]. Here, we present a thermal Hall effect in collinear antiferromagnets without DMI, which may even be present without external fields. While noncollinear antiferromagnets rely exclusively on their magnetic order to break an effective time-reversal symmetry (which is a prerequisite for the thermal Hall effect), collinear antiferromagnets additionally rely on the symmetry-breaking effect of the crystal, e.g., due to nonmagnetic atoms. The underlying mechanism is the magnonic analog of the Hall effect reported in Ref. [84].

**Model and methods.**—We consider a magnet on a two-dimensional (2D) honeycomb lattice (in the  $xy$  plane; depicted in Fig. 1). In the ground state without a magnetic field, the spins of sublattice **A** (**B**) point in the  $+z$  ( $-z$ ) direction.

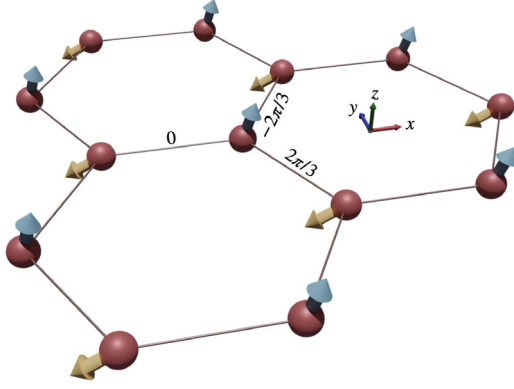


FIG. 1. Honeycomb lattice with antiferromagnetically coupled spins on sublattices A (blue) and B (orange). The spin configuration shown here is paradigmatic for the spin-flop phase with  $A \neq 0$  and a magnetic field applied along  $-z$ .

The spin Hamiltonian

$$\mathcal{H} = \mathcal{H}_{\text{NN}} + \mathcal{H}_{\text{on}} + \mathcal{H}_B \quad (1)$$

comprises the coupling of nearest-neighbor spins,

$$\mathcal{H}_{\text{NN}} = \frac{1}{2\hbar^2} \sum_{\langle ij \rangle} \mathbf{S}_i^T \begin{pmatrix} J + J_a \cos \theta_{ij} & -J_a \sin \theta_{ij} & 0 \\ -J_a \sin \theta_{ij} & J - J_a \cos \theta_{ij} & 0 \\ 0 & 0 & J_z \end{pmatrix} \mathbf{S}_j \quad (2)$$

( $\hbar$  reduced Planck constant). Both in- and out-of-plane spin components are coupled antiferromagnetically, but with different strengths ( $J_z > J > 0$ ). The traceless and symmetric coupling, introduced by  $J_a$ , originates from spin-orbit coupling [85]. It is related to the nearest-neighbor bonds  $\langle ij \rangle$  by the bond-dependent angles  $\theta_{ij} = 0, 2\pi/3$ , and  $-2\pi/3$  (cf. angles near bonds in Fig. 1). The classical collinear configuration favored by  $J$  and  $J_z$  is maintained as long as  $J_a$  is sufficiently small.

This model was proposed for manganese thiophosphate MnPS<sub>3</sub> in Ref. [85] and it produces a nonreciprocal magnon spectrum. Wildes *et al.* did not find signatures of an asymmetric band structure in MnPS<sub>3</sub> and ruled out the presence of DMI [86], another source of nonreciprocity [87]. However, bond-dependent exchange interaction  $J_a$  is allowed by symmetry [85], consistent with results from neutron resonance spin echo spectroscopy [88], and cannot be excluded due to the limited experimental resolution in Ref. [86]. Nevertheless, further insights into the spin-spin interactions are desirable, for example, by comparing experimental results with our predictions for the transport properties.

We extend the model of Ref. [85] by considering an on-site anisotropy

$$\mathcal{H}_{\text{on}} = -\frac{A}{\hbar^2} \sum_{i \in A} (S_i^z)^2 \quad (3)$$

for the spins on sublattice A, which breaks the inversion symmetry on the level of the Hamiltonian. It may be brought about by placing the sample on a substrate or in a heterostructure (e.g., on a transition-metal dichalcogenide), thereby producing local environments of the atoms that differ for the two sublattices [89]. The anisotropy translates into a sublattice-dependent on-site potential of the magnons.

The Zeeman Hamiltonian

$$\mathcal{H}_B = \frac{g\mu_B B_z}{\hbar} \sum_i S_i^z \quad (4)$$

( $g$  is  $g$ -factor,  $\mu_B$  is Bohr magneton) accounts for an out-of-plane magnetic field that destabilizes the antiferromagnetic (AFM) order and induces magnetic phase transitions. Below the critical magnetic field  $B_1^{(m)}$ , defined by

$$g\mu_B B_1^{(m)}/S = \sqrt{(3J_z + A)^2 - 9J^2} - A, \quad (5)$$

the classical ground state is a collinear antiferromagnet with a Néel vector pointing in the  $z$  direction. Between  $B_1^{(m)}$  and  $B_2^{(m)}$ ,

$$g\mu_B B_2^{(m)}/S = 3J_z + \sqrt{9J^2 + A^2} - A, \quad (6)$$

the system is in a coplanar spin-flop (SF) phase, and in the field-polarized (FP) phase (fields larger than  $B_2^{(m)}$ ) all spins point along  $+z$ . The ground state's spin configuration has been obtained by analytical and numerical methods; for details see the Supplemental Material [90].

For the thermal Hall conductivity [38]

$$\kappa_{xy} = -\frac{k_B^2 T}{\hbar V} \sum_{\mathbf{k}} \sum_{n=1}^N c_2[\rho(\varepsilon_{n,\mathbf{k}})] \Omega_{n,\mathbf{k}}, \quad (7)$$

( $T$  temperature,  $k_B$  Boltzmann's constant,  $V$  volume), a large Berry curvature  $\Omega_{n\mathbf{k}}$  at low energies  $\varepsilon_{n\mathbf{k}}$ , which enter the weight function  $c_2[\rho(\varepsilon)]$ , are relevant. More details can be found in the Supplemental Material [90].

We continue with MnPS<sub>3</sub>:  $J_z = 1.541$  meV,  $J = 1.54$  meV,  $J_a = 0.02$  meV, and  $S = 5/2$  [86,94]. Regarding the on-site anisotropy  $A$ , we consider two cases. First, the bulk properties of MnPS<sub>3</sub> are modeled by setting  $A = 0$ . Second, we account for a substrate by setting  $A = 0.1$  meV, which is a realistic value in the range of predictions by *ab initio* calculations for other van der Waals magnets [89]. Our choice for  $A$  renders the respective calculations semiquantitative, since the precise numerical value of  $A$  depends on the selected substrate.

Below, we describe and explain the field-dependent Hall conductivity  $\kappa_{xy}(B_z)$  for increasing field starting at zero. Magnetic ( $m$ ) and topological ( $t$ ) phase transitions occur at  $B_1 < B_2^{(t)} < B_3^{(t)} < B_2^{(m)}$ . If a topological and a magnetic phase transition coincide (e.g., at  $B_1$ ), the notation  $B^{(m)}$  and  $B^{(t)}$  becomes redundant. Changes in  $\kappa_{xy}$  are traced back to the evolution of the magnon spectrum and the Berry curvature. In addition to the descriptions and figures provided here, animations are available in the Supplemental Material [90].

*Discussion of results for bulk MnPS<sub>3</sub>.*—For  $A = 0$  and zero magnetic field, the AFM phase is invariant under simultaneous space inversion  $P$  and time reversal  $T$ , which causes  $\Omega_{n\mathbf{k}} = 0$  and, thus,  $\kappa_{xy} = 0$ . The otherwise degenerate magnon bands are spin-orbit split by  $J_a \neq 0$ , with the exception of the  $\Gamma$  and  $K'$  points in the Brillouin zone (BZ) [85].

A small magnetic field breaks  $PT$  symmetry and lifts the band degeneracies at  $\Gamma$  and  $K'$ , which brings about Berry curvature of opposite sign [ $\Omega_{1\mathbf{k}} > 0$  at  $\Gamma$ ,  $\Omega_{1\mathbf{k}} < 0$  at  $K'$  as displayed in Fig. 3(a)]. The higher thermal occupation of the states around  $\Gamma$  and the minus sign in Eq. (7) explain that  $\kappa_{xy}$  is negative. The higher the temperature, the larger the occupation at  $\Gamma$  and the larger  $|\kappa_{xy}|$ .

As the field strength increases, the positive Berry curvature around  $\Gamma$  is gradually redistributed toward the  $K$  points and the negative Berry curvature at  $K'$  extends toward  $\Gamma$  (cf. Supplemental Material, Video 1 [90]), which explains the nonmonotonic behavior of  $\kappa_{xy}$ .

At the first-order AFM-SF phase transition at  $g\mu_B B_1^{(m)} = 0.416$  meV, also identified by a diverging susceptibility, both **A** and **B** spins are abruptly rotated into the  $xy$  plane but obtain a small (ferromagnetic) component parallel to the magnetic field. In Fig. 2(a), this redirection is seen in the angles  $\theta_A$  and  $\theta_B$  between the  $xy$  plane and the spins (inset: **A** blue, **B** orange) and in the jump of the magnetization from zero to negative values. The experimentally measured critical field in the range of  $g\mu_B B_1 = 0.42$ – $0.54$  meV [97,98] agrees reasonably well with our analysis.

In the SF phase, the lower band is pinned at zero energy at  $\Gamma$  due to the continuous rotational symmetry of the classical ground state energy that is spontaneously broken by the noncollinear ground state [99]. The Berry curvature of band  $n = 1$  is dominantly positive, and the Chern number  $C_1$  jumps from 0 to  $-1$ . Thus, the magnetic phase transition is accompanied by a topological phase transition and  $|\kappa_{xy}|$  is abruptly increased.

Ramping up the magnetic field further, the large Berry curvature around  $\Gamma$  [cf. Fig. 3(b)] becomes redistributed to high-energy magnons [cf. Fig. 3(c)], with the consequence that  $|\kappa_{xy}|$  decreases with the  $B$  field [cf. Fig. 2(b)].

The second topological phase transition at  $g\mu_B B_2^{(t)} = 1.901$  meV is attributed to a band inversion. The Chern numbers of both bands are interchanged; that is,

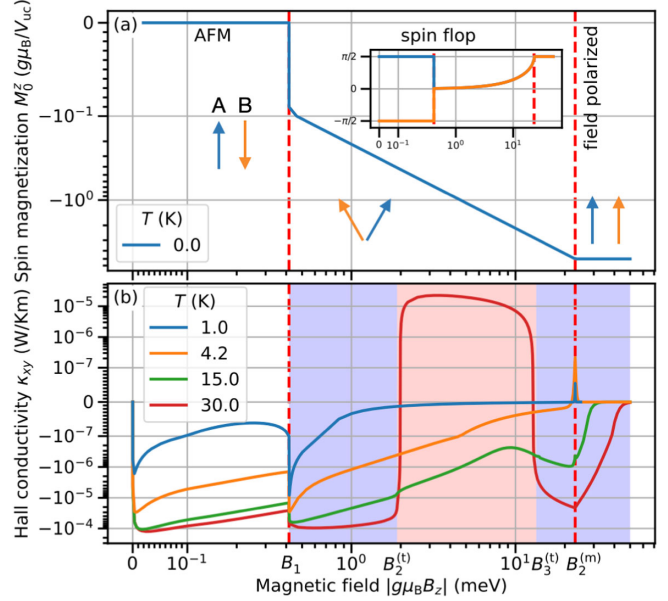


FIG. 2. Magnetic, topological, and transport properties of (bulk) MnPS<sub>3</sub> ( $A = 0$ ). (a) Classical ground state magnetization versus magnetic field. Inset: angles  $\theta_A$  and  $\theta_B$  of the sublattice **A** (blue) and **B** (orange) spins with the  $xy$  plane. (b) Thermal Hall conductivity  $\kappa_{xy}$  for four selected temperatures ( $T = 1.0, 4.2, 15,$  and  $30$  K). The white, blue, red background color indicates topological phases with Chern numbers  $C_1 = 0, -1, +1$  of the lowest magnon band. Dashed red lines mark the magnetic phase transitions at the critical fields  $B_1^{(m)}$  and  $B_2^{(m)}$ . All four panels have logarithmic ordinates and abscissae with linear-scale segments around 0, which are identified by equally spaced minor ticks.

$C_1 = -1 \rightarrow C_1 = +1$ . This band inversion occurs near the BZ edge: just before  $B_2^{(t)}$ , e.g.,  $|g\mu_B B_z| = 1.8$  meV, the dominating positive Berry curvature appears near the BZ edge and is spread along  $k_x$  [red in Fig. 3(c)]. And after the transition, e.g., at  $|g\mu_B B_z| = 2$  meV, this dominating  $\Omega_{n\mathbf{k}}$  has changed sign [blue in Fig. 3(d)]. As a consequence, the band inversion manifests itself in  $\kappa_{xy}$  prominently at elevated temperatures, for which it even causes sign changes [cf. red line in Fig. 2(b)].

The band inversion is reversed again ( $C_1 = +1 \rightarrow C_1 = -1$ ) at  $g\mu_B B_3^{(t)} = 13.368$  meV, again most clearly seen in  $\kappa_{xy}$  at 30 K, which, as before, features a sign change. Approaching  $B_3^{(t)}$  the elongated distribution of the Berry curvature seen for  $B_2^{(t)}$  becomes concentrated around the  $K$  and  $K'$  points, and the band inversion then occurs at these points at the BZ edge (cf. Supplemental Material, Video 1 [90]). In short, the higher the temperature (but still well below the ordering temperature), the stronger  $\kappa_{xy}$  reflects the topological phase transitions.

The second-order magnetic SF-FP phase transition at  $g\mu_B B_2^{(m)} = 23.107$  meV, also identified by a jump in the

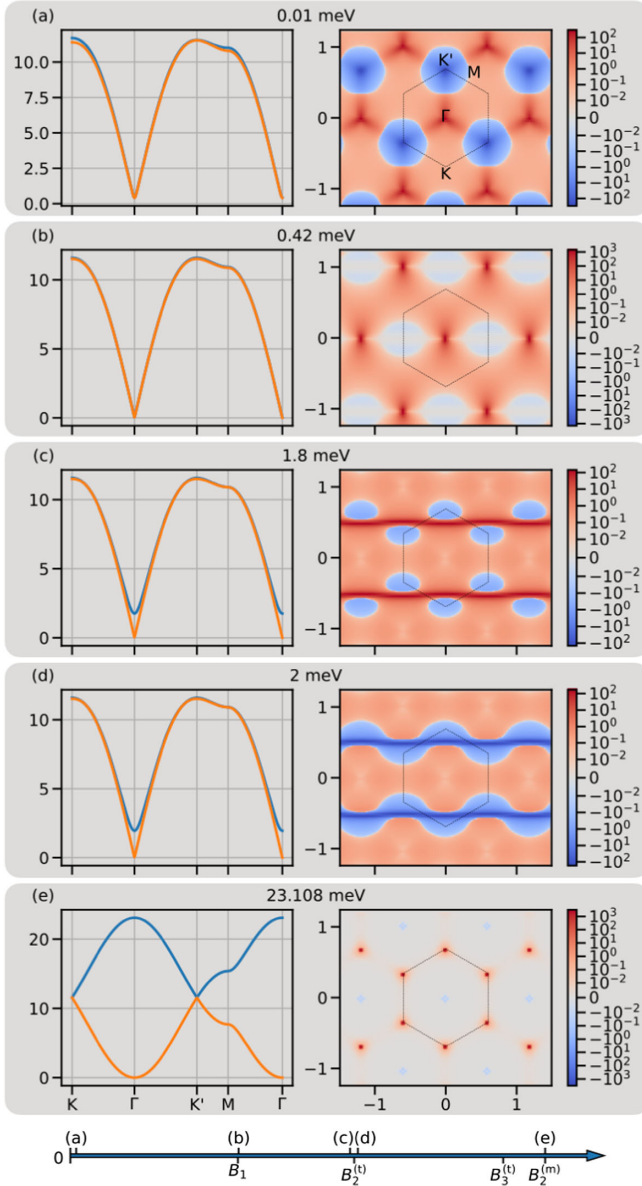


FIG. 3. (a–e) Magnon band structures and Berry curvatures of (bulk)  $\text{MnPS}_3$  ( $A = 0$ ) for selected strengths  $|g\mu_B B_z|$  of the magnetic field. Magnon-dispersion and Berry-curvature panels appear in pairs, indicated by a common gray background, with identical strength of the magnetic field (in meV; the positioning with respect to the phase transitions is sketched at the bottom). The magnon energies  $\varepsilon_{n\mathbf{k}}$  (in meV) are shown along high-symmetry lines of the first Brillouin zone; the Berry curvatures  $\Omega_{1\mathbf{k}}$  of the lowest band are displayed as color maps in reciprocal space (the black hexagons indicate the first BZ). The  $k_x$  and  $k_y$  axes are given in  $\text{\AA}^{-1}$ . Parameters are chosen as in Fig. 2. For an animation, see Supplemental Material, Video 1 [90].

susceptibility, shows clear temperature-dependent signatures in  $\kappa_{xy}$  [Fig. 2(b)]. On the one hand, the dominating positive contribution of the Berry curvature is located at the BZ edges (magnons with higher energies); on the other hand, a small annular, negative contribution shows up near

the BZ center (low-energy magnons) [Fig. 3(e)]. Thus, the weighting between these competing contributions can be altered by the occupation of the respective magnon states and, therefore, by the temperature. To be more specific, low temperatures freeze out the high-energy contribution, allowing the small low-energy contribution to dominate in the transport and leading to a peak with a sign change in  $\kappa_{xy}$ . At elevated temperatures, however, magnons with positive  $\Omega_{n\mathbf{k}}$  are significantly populated. Since the high-energy contribution, being induced by the topological phase transition, exists independently of the magnetic phase transition, it does not show up as a pronounced peak.

At the transition point, the in-plane Néel vector vanishes. The FP phase is hence characterized by a saturated classical magnetization [cf. Fig. 2(a)]. Beyond this second-order transition the magnetic field shifts both bands to higher energies, thereby suppressing thermal transport ( $\kappa_{xy} \rightarrow 0$ ) [Fig. 2(b)].

Based on the above, we conclude that  $\kappa_{xy}$  exhibits clear signatures of magnetic phase transition at low temperatures and of topological phase transitions at higher temperatures.

*Thermal Hall magnetoconductivity.*—The previous analysis revealed the need for a quantity that precisely measures the sensitivity of  $\kappa_{xy}(B_z)$  on the phase transitions. In analogy to the magnetoresistance, we define the thermal Hall magnetoconductivity (THMC) as

$$\text{THMC} = \left| \frac{\kappa_{xy}(\overline{B}_z + \Delta B_z) - \kappa_{xy}(\overline{B}_z - \Delta B_z)}{\kappa_{xy}(\overline{B}_z + \Delta B_z) + \kappa_{xy}(\overline{B}_z - \Delta B_z)} \right|. \quad (8)$$

By definition, the THMC corresponds to the relative change of  $\kappa_{xy}$  upon the phase transition at  $\overline{B}_z$ . In Fig. 4, the THMC is shown versus temperature for (i) the AFM-SF transition (blue line) and (ii) for the topological phase transition at  $B_2^{(t)}$  (orange line) [100]. For (i) the THMC is close to one near 1 K and monotonically decreases with temperature. (ii) The topological phase transition shows the expected behavior, i.e., the THMC is small at low temperatures, indicating that  $\kappa_{xy}$  does not change by much,

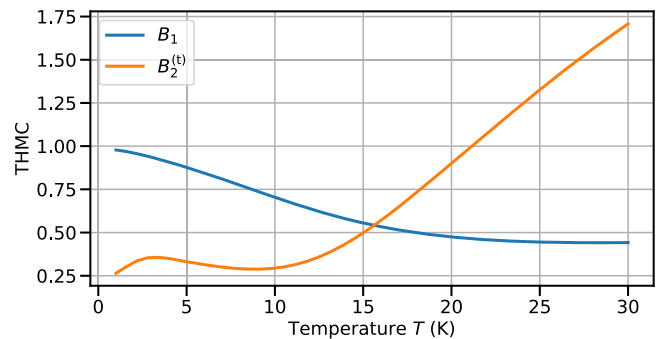


FIG. 4. Thermal Hall magnetoconductivity as a function of temperature  $T$  at the AFM-SF transition  $B_1$  (blue line) and the second topological phase transition  $B_2^{(t)}$  (orange line).

when the topological transition is crossed, but it escalates and takes values close to 175% at 30 K. Based on these results, the drastic changes of  $\kappa_{xy}$  at the phase transitions can be exploited for a “thermal Hall switch,” in which the transverse heat current (or the transverse temperature gradient) is controlled by the external field.

*Results for MnPS<sub>3</sub> on a substrate.*—A substrate or a heterostructure that breaks the sublattice symmetry is mimicked by setting  $A = 0.1$  meV. There are three key differences to bulk MnPS<sub>3</sub> ( $A = 0$ ): (i) The AFM-SF transition becomes continuous. (ii) The nonmagnetic atoms, which are responsible for  $A \neq 0$ , break an effective time-reversal symmetry  $PT$  and a thermal Hall effect in a collinear antiferromagnet without a magnetic field ensues. A similar situation has been reported for the anomalous Hall effect in an electronic system [84]. (iii)  $A$  opens a trivial gap in the FM phase and it dominates over  $J_a$ . Since the AFM phase is always trivial, there are no topological phase transitions. We present the magnon spectra, Berry curvature, thermal Hall effect, and heat capacity for  $A = 0.1$  meV in the Supplemental Material [90].

*Wrap up.*—Our theoretical investigation of the temperature and magnetic-field dependence of the transversal heat conductivity  $\kappa_{xy}$  of a honeycomb magnet proves that  $\kappa_{xy}$  is very sensitive to the magnetic structure at low temperatures: it exhibits pronounced peaks at the magnetic phase transitions, but is rather unaffected by topological phase transitions. Conversely,  $\kappa_{xy}$  traces the topological phase transitions at high temperatures, but is insensitive to the magnetic transitions. Its reading may change several orders near a phase transition and it may also change sign. To paraphrase, magnetic and topological phase transition cause distinct signatures in  $\kappa_{xy}$ , the measurement of which may be used to identify the phase transitions. On the other hand, the strong change under the phase transitions may be exploited as a thermal Hall switch in which the transport properties are manipulated by external means.

Detecting topological (edge) magnons is more difficult than for electrons, since transport of bosons is not quantized—what is a clear signature of nontrivial topology in electronic systems. Instead,  $\kappa_{xy}(B)$  may be investigated as an indicator, its prominent features provide evidence to infer the existence of topological magnons. Although there are other sources of drastic changes in  $\kappa_{xy}(B)$ , a combination with measurements of, e.g., heat capacity  $C_V(B)$ , which is insensitive to topology, could be used to verify the topological nature of the signatures (proof of concept in Supplemental Material [90]).

Our findings call for experimental validation. The numerical results for MnPS<sub>3</sub> suggest that  $\kappa_{xy}$  lies within the experimentally accessible range. We point out that extraordinarily high fields would be required for mapping the entire phase diagram. Nonetheless, the antiferromagnet–spin-flop transition and the topological transition at 2.202 meV are experimentally amenable.

This work is funded by the Deutsche Forschungsgemeinschaft (DFG, German Research Foundation) – Project-ID 328545488 – TRR 227, project B04.

- [1] D. Hsieh, D. Qian, L. Wray, Y. Xia, Y. S. Hor, R. J. Cava, and M. Z. Hasan, A topological Dirac insulator in a quantum spin Hall phase, *Nature (London)* **452**, 970 (2008).
- [2] V. Mourik, K. Zuo, S. M. Frolov, S. R. Plissard, E. P. Bakkers, and L. P. Kouwenhoven, Signatures of Majorana fermions in hybrid superconductor-semiconductor nanowire devices, *Science* **336**, 1003 (2012).
- [3] X.-L. Qi and S.-C. Zhang, Topological insulators and superconductors, *Rev. Mod. Phys.* **83**, 1057 (2011).
- [4] M. Z. Hasan and C. L. Kane, Colloquium: Topological insulators, *Rev. Mod. Phys.* **82**, 3045 (2010).
- [5] X.-B. Li, W.-K. Huang, Y.-Y. Lv, K.-W. Zhang, C.-L. Yang, B.-B. Zhang, Y. B. Chen, S.-H. Yao, J. Zhou, M.-H. Lu, L. Sheng, S.-C. Li, J.-F. Jia, Q.-K. Xue, Y.-F. Chen, and D.-Y. Xing, Experimental Observation of Topological Edge States at the Surface Step Edge of the Topological Insulator ZrTe<sub>5</sub>, *Phys. Rev. Lett.* **116**, 176803 (2016).
- [6] E. Prodan and C. Prodan, Topological Phonon Modes and Their Role in Dynamic Instability of Microtubules, *Phys. Rev. Lett.* **103**, 248101 (2009).
- [7] L. Zhang, J. Ren, J.-S. Wang, and B. Li, Topological Nature of the Phonon Hall Effect, *Phys. Rev. Lett.* **105**, 225901 (2010).
- [8] N. Berg, K. Joel, M. Koolyk, and E. Prodan, Topological phonon modes in filamentary structures, *Phys. Rev. E* **83**, 021913 (2011).
- [9] T. Qin, J. Zhou, and J. Shi, Berry curvature and the phonon Hall effect, *Phys. Rev. B* **86**, 104305 (2012).
- [10] Z.-G. Chen and Y. Wu, Tunable Topological Phononic Crystals, *Phys. Rev. Applied* **5**, 054021 (2016).
- [11] B.-Z. Xia, T.-T. Liu, G.-L. Huang, H.-Q. Dai, J.-R. Jiao, X.-G. Zang, D.-J. Yu, S.-J. Zheng, and J. Liu, Topological phononic insulator with robust pseudospin-dependent transport, *Phys. Rev. B* **96**, 094106 (2017).
- [12] S. Zhang, G. Go, K.-J. Lee, and S. K. Kim, SU(3) Topology of Magnon-Phonon Hybridization in 2D Antiferromagnets, *Phys. Rev. Lett.* **124**, 147204 (2020).
- [13] M. Akazawa, M. Shimozawa, S. Kittaka, T. Sakakibara, R. Okuma, Z. Hiroi, H.-Y. Lee, N. Kawashima, J. H. Han, and M. Yamashita, Thermal Hall Effects of Spins and Phonons in Kagome Antiferromagnet Cd-Kapellasite, *Phys. Rev. X* **10**, 041059 (2020).
- [14] R. Y. Chiao and Y.-S. Wu, Manifestations of Berry’s Topological Phase for the Photon, *Phys. Rev. Lett.* **57**, 933 (1986).
- [15] L. Lu, J. D. Joannopoulos, and M. Soljačić, Topological photonics, *Nat. Photonics* **8**, 821 (2014).
- [16] L. Lu, C. Fang, L. Fu, S. G. Johnson, J. D. Joannopoulos, and M. Soljačić, Symmetry-protected topological photonic crystal in three dimensions, *Nat. Phys.* **12**, 337 (2016).
- [17] T. Ozawa, H. M. Price, A. Amo, N. Goldman, M. Hafezi, L. Lu, M. C. Rechtsman, D. Schuster, J. Simon, O. Zilberberg, and I. Carusotto, Topological photonics, *Rev. Mod. Phys.* **91**, 015006 (2019).

- [18] X.-D. Chen, W.-M. Deng, F.-L. Shi, F.-L. Zhao, M. Chen, and J.-W. Dong, Direct Observation of Corner States in Second-Order Topological Photonic Crystal Slabs, *Phys. Rev. Lett.* **122**, 233902 (2019).
- [19] L. Zhang, J. Ren, J.-S. Wang, and B. Li, Topological magnon insulator in insulating ferromagnet, *Phys. Rev. B* **87**, 144101 (2013).
- [20] A. Mook, J. Henk, and I. Mertig, Magnon Hall effect and topology in kagome lattices: A theoretical investigation, *Phys. Rev. B* **89**, 134409 (2014).
- [21] A. Mook, J. Henk, and I. Mertig, Edge states in topological magnon insulators, *Phys. Rev. B* **90**, 024412 (2014).
- [22] S. A. Owerre, Floquet topological magnons, *J. Phys. Commun.* **1**, 021002 (2017).
- [23] P. A. McClarty, X.-Y. Dong, M. Gohlke, J. G. Rau, F. Pollmann, R. Moessner, and K. Penc, Topological magnons in Kitaev magnets at high fields, *Phys. Rev. B* **98**, 060404(R) (2018).
- [24] A. Rückriegel, A. Brataas, and R. A. Duine, Bulk and edge spin transport in topological magnon insulators, *Phys. Rev. B* **97**, 081106 (2018).
- [25] S. A. Díaz, J. Klinovaja, and D. Loss, Topological Magnons and Edge States in Antiferromagnetic Skyrmion Crystals, *Phys. Rev. Lett.* **122**, 187203 (2019).
- [26] X. S. Wang, A. Brataas, and R. E. Troncoso, Bosonic Bott Index and Disorder-Induced Topological Transitions of Magnons, *Phys. Rev. Lett.* **125**, 217202 (2020).
- [27] R. Mukherjee, R. Kundu, A. Singh, and A. Kundu, Schwinger-boson mean-field study of spin-1/2  $J_1 - J_2 - J_\chi$  model in honeycomb lattice: Thermal Hall signature, [arXiv:2108.08801](https://arxiv.org/abs/2108.08801).
- [28] O. Pietzsch, A. Kubetzka, M. Bode, and R. Wiesendanger, Observation of magnetic hysteresis at the nanometer scale by spin-polarized scanning tunneling spectroscopy, *Science* **292**, 2053 (2001).
- [29] M. Bode, M. Heide, K. V. Bergmann, P. Ferriani, S. Heinze, G. Bihlmayer, A. Kubetzka, O. Pietzsch, S. Blügel, and R. Wiesendanger, Chiral magnetic order at surfaces driven by inversion asymmetry, *Nature (London)* **447**, 190 (2007).
- [30] J. Fernández-Rossier, Theory of Single-Spin Inelastic Tunneling Spectroscopy, *Phys. Rev. Lett.* **102**, 256802 (2009).
- [31] J. Fransson, O. Eriksson, and A. V. Balatsky, Theory of spin-polarized scanning tunneling microscopy applied to local spins, *Phys. Rev. B* **81**, 115454 (2010).
- [32] T. Balashov, A. F. Takács, W. Wulfhekel, and J. Kirschner, Magnon Excitation with Spin-Polarized Scanning Tunneling Microscopy, *Phys. Rev. Lett.* **97**, 187201 (2006).
- [33] J. Feldmeier, W. Natori, M. Knap, and J. Knolle, Local probes for charge-neutral edge states in two-dimensional quantum magnets, *Phys. Rev. B* **102**, 134423 (2020).
- [34] F. Zhu, L. Zhang, X. Wang, F. J. d. Santos, J. Song, T. Mueller, K. Schmalzl, W. F. Schmidt, A. Ivanov, J. T. Park *et al.*, Topological magnon insulators in two-dimensional van der Waals ferromagnets CrSiTe<sub>3</sub> and CrGeTe<sub>3</sub>: Towards intrinsic gap-tunability, *Sci. Adv.* **7** (2021).
- [35] Y. Shiomi, R. Takashima, and E. Saitoh, Experimental evidence consistent with a magnon Nernst effect in the antiferromagnetic insulator MnPS<sub>3</sub>, *Phys. Rev. B* **96**, 134425 (2017).
- [36] H. Katsura, N. Nagaosa, and P. A. Lee, Theory of the Thermal Hall Effect in Quantum Magnets, *Phys. Rev. Lett.* **104**, 066403 (2010).
- [37] Y. Onose, T. Ideue, H. Katsura, Y. Shiomi, N. Nagaosa, and Y. Tokura, Observation of the magnon Hall effect, *Science* **329**, 297 (2010).
- [38] R. Matsumoto and S. Murakami, Rotational motion of magnons and the thermal Hall effect, *Phys. Rev. B* **84**, 184406 (2011).
- [39] R. Matsumoto and S. Murakami, Theoretical Prediction of a Rotating Magnon Wave Packet in Ferromagnets, *Phys. Rev. Lett.* **106**, 197202 (2011).
- [40] R. Shindou, R. Matsumoto, S. Murakami, and J.-i. Ohe, Topological chiral magnonic edge mode in a magnonic crystal, *Phys. Rev. B* **87**, 174427 (2013).
- [41] T. Ideue, Y. Onose, H. Katsura, Y. Shiomi, S. Ishiwata, N. Nagaosa, and Y. Tokura, Effect of lattice geometry on magnon Hall effect in ferromagnetic insulators, *Phys. Rev. B* **85**, 134411 (2012).
- [42] M. Hirschberger, R. Chisnell, Y. S. Lee, and N. P. Ong, Thermal Hall Effect of Spin Excitations in a Kagome Magnet, *Phys. Rev. Lett.* **115**, 106603 (2015).
- [43] R. Matsumoto, R. Shindou, and S. Murakami, Thermal Hall effect of magnons in magnets with dipolar interaction, *Phys. Rev. B* **89**, 054420 (2014).
- [44] X. Cao, K. Chen, and D. He, Magnon Hall effect on the Lieb lattice, *J. Phys. Condens. Matter* **27**, 166003 (2015).
- [45] H. Lee, J. H. Han, and P. A. Lee, Thermal Hall effect of spins in a paramagnet, *Phys. Rev. B* **91**, 125413 (2015).
- [46] B. Xu, T. Ohtsuki, and R. Shindou, Integer quantum magnon Hall plateau-plateau transition in a spin-ice model, *Phys. Rev. B* **94**, 220403(R) (2016).
- [47] K. Nakata, J. Klinovaja, and D. Loss, Magnonic quantum Hall effect and Wiedemann-Franz law, *Phys. Rev. B* **95**, 125429 (2017).
- [48] S. A. Owerre, Topological honeycomb magnon Hall effect: A calculation of thermal Hall conductivity of magnetic spin excitations, *J. Appl. Phys.* **120**, 043903 (2016).
- [49] S. A. Owerre, A first theoretical realization of honeycomb topological magnon insulator, *J. Phys. Condens. Matter* **28**, 386001 (2016).
- [50] S. A. Owerre, Magnon Hall effect in AB-stacked bilayer honeycomb quantum magnets, *Phys. Rev. B* **94**, 094405 (2016).
- [51] S. A. Owerre, Chirality-induced magnon transport in AA-stacked bilayer honeycomb chiral magnets, *J. Phys. Condens. Matter* **28**, 47LT02 (2016).
- [52] A. Mook, J. Henk, and I. Mertig, Spin dynamics simulations of topological magnon insulators: From transverse current correlation functions to the family of magnon Hall effects, *Phys. Rev. B* **94**, 174444 (2016).
- [53] B. Madon, D. C. Pham, J.-E. Wegrowe, D. Lacour, M. Hehn, V. Polewczyk, A. Anane, and V. Cros, Anomalous and planar Righi-Leduc effects in Ni<sub>80</sub>Fe<sub>20</sub> ferromagnets, *Phys. Rev. B* **94**, 144423 (2016).
- [54] A. Okamoto and S. Murakami, Berry curvature for magnons in ferromagnetic films with dipole-exchange interactions, *Phys. Rev. B* **96**, 174437 (2017).

- [55] S. Murakami and A. Okamoto, Thermal Hall effect of magnons, *J. Phys. Soc. Jpn.* **86**, 011010 (2017).
- [56] S. A. Owerre, Topological magnon bands in ferromagnetic star lattice, *J. Phys. Condens. Matter* **29**, 185801 (2017).
- [57] B. Li and A. A. Kovalev, Chiral topological insulator of magnons, *Phys. Rev. B* **97**, 174413 (2018).
- [58] R. Seshadri and D. Sen, Topological magnons in a kagome-lattice spin system with XXZ and Dzyaloshinskii-Moriya interactions, *Phys. Rev. B* **97**, 134411 (2018).
- [59] M. Kawano and C. Hotta, Thermal Hall effect and topological edge states in a square lattice antiferromagnet, *Phys. Rev. B* **99**, 054422 (2019).
- [60] Y.-S. Lu, J.-L. Li, and C.-T. Wu, Topological Phase Transitions of Dirac Magnons in Honeycomb Ferromagnets, *Phys. Rev. Lett.* **127**, 217202 (2021).
- [61] F. Zhuo, H. Li, and A. Manchon, Topological phase transition and thermal Hall effect in kagome ferromagnets, *Phys. Rev. B* **104**, 144422 (2021).
- [62] M. Hirschberger, J. W. Krizan, R. J. Cava, and N. P. Ong, Large thermal Hall conductivity of neutral spin excitations in a frustrated quantum magnet, *Science* **348**, 106 (2015).
- [63] K. A. van Hoogdalem, Y. Tserkovnyak, and D. Loss, Magnetic texture-induced thermal Hall effects, *Phys. Rev. B* **87**, 024402 (2013).
- [64] C. Schütte and M. Garst, Magnon-skyrmion scattering in chiral magnets, *Phys. Rev. B* **90**, 094423 (2014).
- [65] A. Mook, B. Göbel, J. Henk, and I. Mertig, Magnon transport in noncollinear spin textures: Anisotropies and topological magnon Hall effects, *Phys. Rev. B* **95**, 020401 (R) (2017).
- [66] S. A. Owerre, Topological thermal Hall effect in frustrated kagome antiferromagnets, *Phys. Rev. B* **95**, 014422 (2017).
- [67] S. A. Owerre, Magnon Hall effect without Dzyaloshinskii-Moriya interaction, *J. Phys. Condens. Matter* **29**, 03LT01 (2017).
- [68] S. A. Owerre, Topological magnetic excitations on the distorted kagome antiferromagnets: Applications to volborthite, vesignieite, and edwardsite, *Europhys. Lett.* **117**, 37006 (2017).
- [69] S. A. Owerre, Noncollinear antiferromagnetic Haldane magnon insulator, *J. Appl. Phys.* **121**, 223904 (2017).
- [70] E. Iacocca and O. Heinonen, Topologically Nontrivial Magnon Bands in Artificial Square Spin Ices with Dzyaloshinskii-Moriya Interaction, *Phys. Rev. Applied* **8**, 034015 (2017).
- [71] K. Hwang, N. Trivedi, and M. Randeria, Topological Magnons with Nodal-Line and Triple-Point Degeneracies: Implications for Thermal Hall Effect in Pyrochlore Iridates, *Phys. Rev. Lett.* **125**, 047203 (2020).
- [72] P. Laurell and G. A. Fiete, Topological Magnon Bands and Unconventional Superconductivity in Pyrochlore Iridate Thin Films, *Phys. Rev. Lett.* **118**, 177201 (2017).
- [73] P. Laurell and G. A. Fiete, Magnon thermal Hall effect in kagome antiferromagnets with Dzyaloshinskii-Moriya interactions, *Phys. Rev. B* **98**, 094419 (2018).
- [74] S. Owerre, Topological thermal Hall effect due to Weyl magnons, *Can. J. Phys.* **96**, 1216 (2018).
- [75] J. Cookmeyer and J. E. Moore, Spin-wave analysis of the low-temperature thermal Hall effect in the candidate Kitaev spin liquid  $\alpha$ -RuCl<sub>3</sub>, *Phys. Rev. B* **98**, 060412 (R) (2018).
- [76] S. K. Kim, K. Nakata, D. Loss, and Y. Tserkovnyak, Tunable Magnonic Thermal Hall Effect in Skyrmion Crystal Phases of Ferrimagnets, *Phys. Rev. Lett.* **122**, 057204 (2019).
- [77] A. Mook, J. Henk, and I. Mertig, Thermal Hall effect in noncollinear coplanar insulating antiferromagnets, *Phys. Rev. B* **99**, 014427 (2019).
- [78] D. Watanabe, K. Sugii, M. Shimozawa, Y. Suzuki, T. Yajima, H. Ishikawa, Z. Hiroi, T. Shibauchi, Y. Matsuda, and M. Yamashita, Emergence of nontrivial magnetic excitations in a spin-liquid state of kagomé volborthite, *Proc. Natl. Acad. Sci. U.S.A.* **113**, 8653 (2016).
- [79] Y. Kasahara, K. Sugii, T. Ohnishi, M. Shimozawa, M. Yamashita, N. Kurita, H. Tanaka, J. Nasu, Y. Motome, T. Shibauchi, and Y. Matsuda, Unusual Thermal Hall Effect in a Kitaev Spin Liquid Candidate  $\alpha$ -RuCl<sub>3</sub>, *Phys. Rev. Lett.* **120**, 217205 (2018).
- [80] Y. Kasahara, T. Ohnishi, Y. Mizukami, O. Tanaka, S. Ma, K. Sugii, N. Kurita, H. Tanaka, J. Nasu, Y. Motome *et al.*, Majorana quantization and half-integer thermal quantum Hall effect in a Kitaev spin liquid, *Nature (London)* **559**, 227 (2018).
- [81] H. Doki, M. Akazawa, H.-Y. Lee, J. H. Han, K. Sugii, M. Shimozawa, N. Kawashima, M. Oda, H. Yoshida, and M. Yamashita, Spin Thermal Hall Conductivity of a Kagome Antiferromagnet, *Phys. Rev. Lett.* **121**, 097203 (2018).
- [82] R. Hentrich, M. Roslova, A. Isaeva, T. Doert, W. Brenig, B. Büchner, and C. Hess, Large thermal Hall effect in  $\alpha$ -RuCl<sub>3</sub>: Evidence for heat transport by Kitaev-Heisenberg paramagnons, *Phys. Rev. B* **99**, 085136 (2019).
- [83] M. Yamashita, M. Akazawa, M. Shimozawa, T. Shibauchi, Y. Matsuda, H. Ishikawa, T. Yajima, Z. Hiroi, M. Oda, H. Yoshida, H.-Y. Lee, J. H. Han, and N. Kawashima, Thermal-transport studies of kagomé antiferromagnets, *J. Phys. Condens. Matter* **32**, 074001 (2020).
- [84] L. Šmejkal, R. González-Hernández, T. Jungwirth, and J. Sinova, Crystal time-reversal symmetry breaking and spontaneous Hall effect in collinear antiferromagnets, *Sci. Adv.* **6**, eaaz8809 (2020).
- [85] T. Matsumoto and S. Hayami, Nonreciprocal magnons due to symmetric anisotropic exchange interaction in honeycomb antiferromagnets, *Phys. Rev. B* **101**, 224419 (2020).
- [86] A. R. Wildes, S. Okamoto, and D. Xiao, Search for nonreciprocal magnons in MnPS<sub>3</sub>, *Phys. Rev. B* **103**, 024424 (2021).
- [87] R. Cheng, S. Okamoto, and D. Xiao, Spin Nernst Effect of Magnons in Collinear Antiferromagnets, *Phys. Rev. Lett.* **117**, 217202 (2016).
- [88] T. J. Hicks, T. Keller, and A. R. Wildes, Magnetic dipole splitting of magnon bands in a two dimensional antiferromagnet, *J. Magn. Magn. Mater.* **474**, 512 (2019).
- [89] R. Hidalgo-Sacoto, R. I. Gonzalez, E. E. Vogel, S. Allende, J. D. Mella, C. Cardenas, R. E. Troncoso, and F. Muñoz, Magnon valley Hall effect in CrI<sub>3</sub>-based van der Waals heterostructures, *Phys. Rev. B* **101**, 205425 (2020).
- [90] See Supplemental Material at <http://link.aps.org/supplemental/10.1103/PhysRevLett.128.117201>, which contains the parameters of MnPS<sub>3</sub>, details on the theoretical

- calculations, results for the spin texture in the spin-flop phase, on order-by-disorder, and the pseudo-Goldstone gaps, on heat capacity, and transport calculations for enhanced spin-orbit parameter  $J_a$ . The Supplemental Material also includes videos that show the evolution of the magnon spectra (top left panel) and the Berry curvatures of both bands (lowest band, top right panel; highest band, bottom right panel) for different parameter sets as the magnetic field is varied (bottom left panel). The Supplemental Material includes Refs. [38,77,84, 86,91–96].
- [91] T. Holstein and H. Primakoff, Field dependence of the intrinsic domain magnetization of a ferromagnet, *Phys. Rev.* **58**, 1098 (1940).
- [92] A. Jain, S. P. Ong, G. Hautier, W. Chen, W. D. Richards, S. Dacek, S. Cholia, D. Gunter, D. Skinner, G. Ceder, and K. Persson, The Materials Project: A materials genome approach to accelerating materials innovation, *APL Mater.* **1**, 011002 (2013).
- [93] K. Persson, Materials data on  $\text{MnPS}_3$  (sg:12) by materials project (2016), [10.17188/1309185](https://doi.org/10.17188/1309185).
- [94] A. R. Wildes, B. Roessli, B. Lebech, and K. W. Godfrey, Spin waves and the critical behaviour of the magnetization in  $\text{MnPS}_3$ , *J. Phys. Condens. Matter* **10**, 6417 (1998).
- [95] J. G. Rau, P. A. McClarty, and R. Moessner, Pseudo-Goldstone Gaps and Order-by-Quantum Disorder in Frustrated Magnets, *Phys. Rev. Lett.* **121**, 237201 (2018).
- [96] R. R. Neumann, A. Mook, J. Henk, and I. Mertig, Orbital Magnetic Moment of Magnons, *Phys. Rev. Lett.* **125**, 117209 (2020).
- [97] K. Okuda, K. Kurosawa, S. Saito, M. Honda, Z. Yu, and M. Date, Magnetic properties of layered compound  $\text{MnPS}_3$ , *J. Phys. Soc. Jpn.* **55**, 4456 (1986).
- [98] D. J. Goossens and T. J. Hicks, The magnetic phase diagram of  $\text{Mn}_x\text{Zn}_{1-x}\text{PS}_3$ , *J. Phys. Condens. Matter* **10**, 7643 (1998).
- [99] We neglect a pseudo-Goldstone gap [95] that we show to be irrelevant in the Supplemental Material [90].
- [100] We have set  $\overline{B}_z = B_1$  and  $\Delta B_z = 2 \mu\text{eV}$  for (i) and  $\overline{B}_z = B_2^{(t)}$  and  $\Delta B_z = 0.4 \text{ meV}$  for (ii).